PAPER

Check for updates

NIR-II emissive donor–acceptor–donor fluorophores for dual fluorescence bioimaging and photothermal therapy applications†‡

Nicholas E. Sparks,[a] Cameron Smith, [ID][c] Terrence Stahl,[a] Dhanush L. Amarasekara,[d] Christine Hamadani, [ID][c] Ethan Lambert, [ID][c] Sheng Wei Tang,[a] Anuja Kulkarni,[a] Blaine M. Derbigny,[a] Gaya S Dasanayake, [ID][c] George Taylor,[c] Maryam Ghazala,[a] Nathan I. Hammer, [ID][c] Alexander Y. Sokolov, [ID][a] Nicholas C. Fitzkee, [ID][d] Eden E. L. Tanner [ID][c] and Davita L. Watkins [ID]★[ab]

Fluorescence bioimaging with near-infrared II (NIR-II) emissive organic fluorophores has proven to be a viable noninvasive diagnostic technique. However, there is still the need for the development of fluorophores that possess increased stability as well as functionalities that impart stimuli responsiveness. Through strategic design, we can synthesize fluorophores that possess not only NIR-II optical profiles but also pH-sensitivity and the ability to generate heat upon irradiation. In this work, we employ a donor–acceptor–donor (D–A–D) design to synthesize a series of NIR-II fluorophores. Here we use thienothiadiazole (TTD) as the acceptor, 3-hexylthiophene (HexT) as the π-spacer and vary the alkyl amine donor units: *N,N*-dimethylaniline (DMA), phenylpiperidine (Pip), and phenylmorpholine (Morp). Spectroscopic analysis shows that all three derivatives exhibit emission in the NIR-II region with λ_{max}^{emi} ranging from 1030 to 1075 nm. Upon irradiation, the fluorophores exhibited noticeable heat generation through non-radiative processes. The ability to generate heat indicates that these fluorophores will act as theranostic (combination therapeutic and diagnostic) agents in which simultaneous visualization and treatment can be performed. Additionally, biosensing capabilities were supported by changes in the absorbance properties while under acidic conditions as a result of protonation of the alkyl amine donor units. The fluorophores also show minimal toxicity in a human mammary cell line and with murine red blood cells. Overall, initial results indicate viable NIR-II materials for multiple biomedical applications.

Introduction

Near-infrared-II (NIR-II, 1000–1700 nm) emissive materials are of great interest for a variety of applications ranging from organic electronics to biomedical applications.[1–3] Recently, fluorescence bioimaging has seen a resurgence in popularity as an alternative to magnetic resonance imaging (MRI) and computed tomography (CT). This imaging technique allows for

[a] *Department of Chemistry and Biochemistry, The Ohio State University, Columbus, Ohio 43210, USA. E-mail: watkins.891@osu.edu*

[b] *William G. Lowrie Department of Chemical and Biomolecular Engineering, The Ohio State University, 151 W Woodruff Ave., Columbus, OH 43210, USA*

[c] *Department of Chemistry and Biochemistry, University of Mississippi University, Oxford, MS, USA*

[d] *Department of Chemistry, Mississippi State University, Mississippi State, MS 39762, USA*

† This paper is dedicated to the memory of Maria P. Jeffrey.

‡ Electronic supplementary information (ESI) available. See DOI: https://doi.org/10.1039/d3tc04747d

noninvasive monitoring of physiological processes, which can result in more precise diagnosis and treatment of disease.[4,5] More specifically, NIR-II emissive organic fluorophores have found favor in performing this task, and there are numerous publications detailing the benefits of using these compounds.[6]

Utilizing NIR-II emissive organic fluorophores allows for decreased backscattering of emitted photons which increases the resolution of the resulting images.[7,8] Fluorescence imaging in the NIR-II with organic fluorophores also increases the signal-to-background noise ratio, as the intrinsic fluorescence of human tissues is significantly reduced in the NIR-II.[9] There is also an observed increase in penetration depth when using NIR-II organic fluorophores due to the optical transparency of superficial tissues in the NIR-II window.[10,11] Although NIR-II emissive fluorophores are shown to possess superior photophysical properties, there are currently none undergoing clinical trials. As such, the only two FDA-approved organic fluorophores for bioimaging applications are indocyanine green (ICG) and methylene blue (MB), both

This journal is © The Royal Society of Chemistry 2024

J. Mater. Chem. C, 2024, **12**, 4369–4383 | **4369**

of which are NIR-I emissive and face multiple issues with *in vivo* applications.[12–15]

Numerous design strategies are employed to synthesize NIR-II emissive compounds.[16] Perhaps the most promising design strategy with regard to enhanced photophysical properties along with synthetic feasibility is that of the donor–acceptor–donor (D–A–D) motif.[17] The D–A–D strategy allows for control of the energy gap between the highest occupied molecular orbital (HOMO) and the lowest unoccupied molecular orbital (LUMO).[18] Using electron donors and electron acceptors with appropriate HOMO and LUMO energies, fluorophores with NIR-II emissive properties can be achieved as a result of intramolecular charge transfer (ICT) processes.[19]

Choosing the correct acceptor is perhaps the most critical choice in the design of D–A–D NIR-II emissive fluorophores. To date, the most successful acceptor used in NIR-II D–A–D fluorophores is benzobisthiadiazole (BBTD).[20] This polycyclic acceptor has been shown to have pro-quinoidal characteristics, a low-energy conformation observed with fluorophores exhibiting ICT. BBTD favors this form over the alternative benzenoid structure due to the hypervalent sulfur atom present in the benzenoid form (–N=S=N–). The quinoid structure relaxes the hypervalent sulfur through rearrangement of the double bonds, which provides a more classic bonding form (=N–S–N=).[21] Since the quinoid structure is achieved upon the excitation of an electron from the HOMO to the LUMO, the increased stability associated with the quinoidal form allows for low-energy excitations. Interestingly, the quinoid form has also been hypothesized to exist in the ground state as measured through theoretical bond length measurements.[22]

Although BBTD is a well-studied acceptor in NIR-II emissive fluorophores, there is still the need to find alternative electron-accepting moieties for D–A–D compounds. A potential alternative is thienothiadiazole (TTD), which is a similar type of acceptor to BBTD but has not been as extensively studied as a small molecule fluorophore, often relegated to the field of organic electronics.[23,24] Despite its more favorable synthetic accessibility, to date, only one publication has employed TTD as an acceptor moiety, resulting in NIR-II emissive D–A–D fluorophores.[25] The NIR-II emissive properties of the fluorophores resulted from the extended conjugation length and, thus, narrow HOMO–LUMO gaps.[25] Although extension of the conjugated framework is an effective method to red-shift optical properties into the NIR-II, it can result in increased intermolecular interactions and diminished photophysical performance for bioimaging purposes.[26] Previously, we synthesized a series of TTD-based fluorophores that utilized the aryl amine carbazole as the donor unit, which had emission maxima of 900 nm with the emission bands extending into the NIR-II.[27] We utilized electron paramagnetic resonance spectroscopy (EPR) to rationalize differences in quantum yield values and provided evidence of radical species on the TTD-based small molecule fluorophores. Despite possessing both an excellent acceptor and donor, these studies highlighted the effects of sterics, competing transitions, and efficient π-contribution on NIR-II fluorophore design and application.
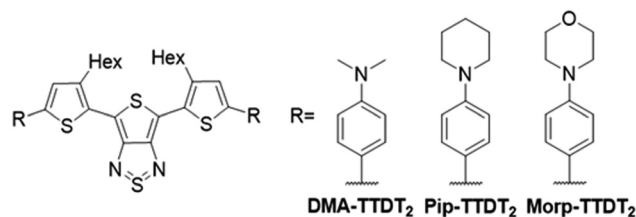

Fig. 1 Structures of the three title compounds, DMA-TTDT$_2$, Pip-TTDT$_2$, and Morp-TTDT$_2$.

Motivated by this, we sought to study the effects of using different amine donors, specifically alkyl aniline derivatives. Computational studies support that alkyl aniline donors contribute more effectively to bathochromic shifts in emission maxima than their aryl amine counterparts.[28] Herewith, we manipulated the photophysical properties by varying the electron donor strength to achieve a series of TTD-based fluorophores that utilize dimethylaniline (DMA), phenylmorpholine (Morp), and phenylpiperidine (Pip) as the electron donor moieties with hexyl thiophene (T$_2$) as the π-spacer (Fig. 1). The title compounds, **DMA-TTDT$_2$**, **Morp-TTDT$_2$**, and **Pip-TTDT$_2$**, all exhibit emission in the NIR-II region. Additionally, the fluorophores exhibited pH-sensitivity and photothermal properties, extending their use into biosensing and theranostic applications. Encapsulation of the fluorophores into a novel amphiphilic copolymer (PhPCL-PEG) further illustrated their unique properties for simultaneous diagnosis and therapy. The high biocompatibility of the nanoparticles was demonstrated with cytotoxicity studies with human mammary cells and murine red blood cells. The detailed synthesis and characterization of the fluorophores and the fluorophore-polymer nanoparticles are described to highlight their potential as promising materials for NIR-II fluorescence bioimaging.[29,30]

Materials and instrumentation

Reagents and solvents were purchased from commercial sources and were used without further purification. Anhydrous solvents were obtained from a Glass Contour (Irvine, CA, USA) solvent system. Thin-layer chromatography was performed using SiO2-60 F254 aluminum plates with visualization by ultraviolet (UV) light. Flash column chromatography was performed using a Purasil SiO2-60, 230–400 mesh from Whatman. Nuclear magnetic resonance (NMR) spectra were obtained on a Bruker (Milton, ON, Canada) 600 MHz spectrometer with the appropriate deuterated solvents. Electron paramagnetic resonance (EPR) spectroscopy was performed with a Bruker (Milton, ON, Canada) Magnettech ESR5000 spectrometer with 1 mM solutions (CDCl$_3$) of each fluorophore.

Computational methods

Absorption and emission calculations were performed for **DMA-TTDT$_2$**, **Morp-TTDT$_2$**, and **Pip-TTDT$_2$** fluorophores, where hexyl groups on the thiophene spacers were replaced with methyl groups. The S$_0$ and S$_1$ geometries of the compounds were optimized using the CAM-B3LYP density functional with

4370 | *J. Mater. Chem. C*, 2024, **12**, 4369–4383

This journal is © The Royal Society of Chemistry 2024

the cc-pVDZ basis set.[31–33] The calculations were carried out using an unrestricted reference wavefunction. The stability of reference wavefunction was checked using a stability analysis. Time-dependent density functional theory (TDDFT) was used to perform all excited state calculations.[34] The TDDFT calculations employed the CAM-B3LYP functional and a modified basis set where all heteroatoms had additional diffuse basis functions (aug-cc-pvdz).[32,33,35] The solvent effects were described using a polarizable continuum model (PCM) with chloroform as a solvent.[36] For each electronic transition in TDDFT, we calculated natural transition orbitals (NTOs), which were used to quantify and visualize the orbital contributions from the amine donor and thiophene spacers.[37] Finally, natural bond orbital calculations were performed to obtain the atomic charge for all nitrogen atoms.[38] All calculations utilized the Ohio Supercomputer Center and the Q-chem quantum chemistry package.[39,40] Full computational data can be found in the ESI‡ in the computational assessment section.

Photophysical assessment

Absorption measurements were carried out on a Varian Cary-500 spectrometer (Dorval, OC, Canada) in $CHCl_3$. Transient absorption measurements (TAS) were performed with a 1 kHz regeneratively amplified Ti:Sapphire laser (Coherent Astrella, Santa Clara, California) with a 7 W, 100 fs output pulse centered at 800 nm output is split with an 85–15 beam splitter to generate pump and probe beams. To generate the pump, the reflected portion of the 800 nm output is directed into a commercial optical parametric amplifier (OPerA Solo, Vilnius, Lithuania), producing a 650 nm pump beam. Both the output of the OPerA Solo as well as the remainder of the originally transmitted 800 nm light are directed into a commercial transient absorption spectrometer (Ultrafast Systems Helios, Sarasota, Florida). The pump beam is chopped at 500 Hz before being depolarized and focused with a 350 mm focal length lens to the sample position. The remaining 800 nm light is first passed onto a mechanical delay stage before being focused onto a translating CaF_2 crystal to generate a visible white light continuum from 425 to 850 nm. The white light is then filtered to remove any remaining fundamental light and split into the probe and reference beams. The reference beam is then reflected into a separate camera to account for jitter and intensity fluctuations. Ultrafast data ($\Delta OD(\lambda, t)$) for each sample were collected by averaging 3 scans with 2 s of averaging at each time delay and corrected with a polynomial to account for the temporal chirp. Samples were held in 2 mm quarts cuvettes (FireflySci, Inc., Staten Island, New York). Single wavelength kinetics $\Delta OD(\lambda_{max}, t)$ were fit with either a single exponential (eqn (1)) or a biexponential decay function (eqn (2)) depending on the photophysical dynamics within the system.

$$\Delta OD(\lambda_{max}, t) = A e^{\frac{-(x-x_0)}{\tau}} \quad (1)$$

$$\Delta OD(\lambda_{max}, t) = A_1 e^{\frac{-(x-x_0)}{\tau_1}} + A_2 e^{\frac{-(x-x_0)}{2}} \quad (2)$$

where A represents of either the individual or total lifetime τ.

For the biexponential kinetics, an average lifetime τ_{avg} is calculated by eqn (3).

$$\tau_{avg} = \frac{A_1 \tau_1 + A_2 \tau_2}{A_1 + A_2} \quad (3)$$

The steady-state emission data was collected using a Horiba PTI QuantaMaster QM-8075-21 fluorometer equipped with both a silicon-based PhotoMultiplier Tube (PMT) in the visible and Near Infrared (NIR) region (425 to 950 nm) while liquid nitrogen cooled Indium Gallium Arsenide (InGaAs) detector was used in the NIR-I and NIR-II (950 to 1400 nm). For both the free and encapsulated dyes (solvents of chloroform and Milli-Q water, respectively), IR-1061 in DCM ($\Phi = 0.32\%$, Cosco) was used to calculate relative fluorescent quantum yield.[41] Absorption and emission blanks of the relevant solvents were subtracted from subsequent dye absorption and emission. Sample and reference concentration was kept below 1 Abs unit to minimize inner filter effects (Levitus).[42] Rectangular 10 mm path cuvettes were used for all fluorescence measurements under ambient atmosphere. The photoluminescent quantum yields (PLQY) of the dyes were determined using the integrated emission intensity values (summation of all Y-value data points using Microsoft Excel) by using the relative quantum yield equation:

$$\Phi_{sample} = \Phi_{reference} \times \frac{E_{sample}}{E_{reference}} \times \frac{S_{reference}}{S_{sample}} \times \frac{\eta_{sample}^2}{\eta_{reference}^2} \quad (4)$$

where Φ denotes the quantum yield; E refers to integrated emission intensity; S is equal to $1-10^{-A}$, with the superscript A being the absorbance value at the excitation wavelength; η is the refractive index of the solvent; sample is the dye studied herein, and reference is the reference standard chosen for quantum yield studies. For measurements made in the NIR/SWIR region, 823 nm was chosen as the excitation wavelength (1 nm step size, 0.5 second integration, and 10 nm resolution for excitation and emission) from a 75 W Xenon arc lamp.

Nanoparticle loading and assessment

Encapsulation of the fluorophores was done using the thin-film nanoparticle formation method. Separate 1 mg mL^{-1} solutions were prepared with respect to polymer/water ratios. 1 mg of fluorophore and 2 mg of the polymer were thoroughly dissolved in 0.3 mL of DCM and 0.3 mL of acetone (0.6 mL total). The organic solvent was evaporated by a gentle flow of N_2, and the resulting nanoparticles were formed by reconstituting with 2 mL of MilliQ water. The nanoparticle solutions were then allowed to equilibrate overnight, followed by filtration through 0.45-micron syringe filters to afford the final nanoparticle solutions. The blank polymer nanoparticle solutions were prepared similarly.

Dynamic light scattering (DLS) and transmission electron microscopy (TEM) were used to characterize the morphological properties of the encapsulated fluorophores. Particle size and polydispersity index (PDI) were measured utilizing a Malvern Instrument Zetasizer Nano ZS using a 633 nm wavelength

He–Ne laser with a detector angle of 173° at 25 °C. For DLS, the samples were used without any treatment or dilution.

Electron microscopy was performed at the Center for Electron Microscopy and Analysis (CEMAS) at The Ohio State University. Grids were imaged on a Tecnai F20 TEM (Thermo-Fisher Scientific) at an accelerating voltage of 200 kV with a Gatan Orius CCD camera. Carbon-coated 300 mesh copper grids were glow-discharged at 20 mA for 10 seconds. Samples were diluted to a concentration of 0.1 mg mL^{-1} in distilled water. After dilution, 3 μL of the sample was added to the grids and allowed to adhere for 1 minute. Grids were washed twice in distilled water and stained in Uranyless EM Stain (Electron Microscopy Sciences, Hatfield, PA) for 1 minute. Grids were blotted dry and stored until imaging.

Photothermal efficiency

To measure the photothermal conversion efficiency (η), the fluorophore-encapsulated nanoparticles (1 mL) were irradiated by an 808 nm laser (0.4 W). The temperature change of the solution was recorded by an IR thermal camera (PI400i, Optris, Portsmouth, NH), and the η was calculated using the following formulas.[43–45]

$$\theta = \frac{T - T_{sur}}{T_{max} - T_{sur}} \tag{5}$$

$$\tau = -\frac{t}{\ln(\theta)} \tag{6}$$

$$Q = \frac{\left[mc\left(T_{max,water} - T_{surr}\right)\right]}{\tau} \tag{7}$$

$$\eta = \frac{Q_{nanoparticles} - Q_{water}}{I\left(1 - 10^{-A_{808}}\right)} \tag{8}$$

In these formulas, T_{max} is the maximum steady state temperature of the solution during irradiation, T_{sur} is the temperature of the surrounding environment, Q_{water} is the heat dissipation from the light absorbed by the solvent and the container, I is the laser power, A_{808} is the absorbance of the dye encapsulated nanoparticles at 808 nm (1 cm path length), m is the mass (1 g), c is the heat capacity (4.2 J g^{-1} K^{-1}) of the solvent, and τ is the thermal time constant. To calculate τ, the cooling curve was examined after removing laser irradiation. Temperature *vs.* time data from the cooling period was used to calculate the thermal time constant (τ) by fitting a 1st order exponential decay to the data. Alternatively, eqn (6) can be used to determine τ from the slope of a line of $\ln(\theta)$ *vs. t*. Then, Q_{water} was calculated *via* eqn (7), which calculates the background energy input in the absence of fluorophore-encapsulated nanoparticles. Three measurements of η were performed using independent samples, and the average and standard error of the mean were reported.

Biological assessment

Cell viability was assessed using Promega's CellTiter-Glo luminescent assay kit with MDA-MB-231 (triple-negative breast cancer, TNBC) and MCF-10A cells (non-tumorigenic human breast cells). The viability was measured after exposing the cells to seven different nanoparticle concentrations for 24 h in a 96-well plate (seeded with 2×10^4 cells per well) at 37 °C and the luminescence readings were carried out on a UV-Vis/fluorescent plate reader (Biotek H1 Synergy Hybrid Multi-mode).[46] The percentage cell viability was determined and presented as the ratio of fluorescence to the negative control (cells only).

To evaluate the possible nanoparticle biocompatibility profile in systemic circulation, red blood cell (RBC) hemolysis was evaluated in quadruplicate, as previously described.[47–49] Briefly, 1 mg mL^{-1} PhPCL-PEG polymeric nanoparticles in 1× PBS pH 7.4 (either empty or with fluorophore encapsulated) were combined in a 96-well clear Greiner plate at 0.05, 0.1, and 0.2 mg mL^{-1} with washed and isolated murine BALB/c RBCs (whole gender-pooled BALB/c mouse blood derived from Bio-IVT, USA & RBCs formulated at a 1 : 50 v/v stock). 20% Triton X-100 was designated as the positive hemolytic control, and 1× PBS pH 7.4 was designated as the negative hemolytic control treatment. These treatment concentrations respectively correlate to doses of 1 : 20 v/v, 1 : 10 v/v, and 1 : 5 v/v, for a final volume of 200 μL per well.

After aspirating *via* pipette to mix thoroughly in each well, all control & nanoparticle-treated RBC samples were then incubated for 1 hour at 37 °C, and then the entire plate was centrifuged at 4 °C for 10 minutes at $500 \times g$ (Thermo Scientific Sorvall X Pro Series Centrifuge, #Sorvall X1R Pro-MD). 100 μL of supernatant was then collected and transferred to a new 96-well clear plate to measure peak hemolytic absorbance in quadruplicate at an experimentally determined 410 nm by a Cytation 5 imaging plate reader (Agilent technologies, #CYT5MF). For analysis, readout from 1× PBS pH 7.4 was subtracted as a minimum baseline (0%) from all samples, and the Triton-X-100 positive control was used as a maximum baseline (100%) to calculate normalized hemolytic percentages with standard deviation ($n = 4$). A paired two-tail *t*-test of means was used to determine significance between 2 samples at a time, while a one-way ANOVA determined significance for 3 or more samples at a time.

Design and synthesis

DMA-TTDT$_2$ and **Morp-TTDT$_2$** were synthesized in over six steps, while **Pip-TTDT$_2$** was synthesized in seven steps, resulting in yields ranging from 31% to 38%. The TTDT$_2$ and TTDT$_2$-Br$_2$ intermediates were synthesized according to previously established procedures.[50,51] The alkyl amine donors were chosen as they are shown to be more effective π-donors than their aryl amine counterparts. This is attributed to decreased steric effects of the less bulky alkyl amine units, which effectively extends the conjugation of the fluorophore and narrows HOMO–LUMO gaps.[28] Additionally, alkyl amines have been utilized as selective targeting and sensing moieties; thus, enhancing the potential applicability of these fluorophores as molecular probes with "on–off" emissions.[52,53]

The DMA and Morp donor precursors were produced from commercially available reagents by performing lithium–halogen

4372 | *J. Mater. Chem. C*, 2024, **12**, 4369–4383

This journal is © The Royal Society of Chemistry 2024

exchange reactions and subsequent stannylations with the brominated starting materials. The Pip donor was achieved by taking 4-bromoaniline and performing an intramolecular alkylation according to an established procedure followed by the corresponding lithium halogen exchange and stannylation reactions. The title compounds were then synthesized under standard Stille coupling conditions by reacting TTDT$_2$-Br$_2$ and the stannylated donor intermediates. We chose to use an amphiphilic diblock copolymer to increase water accessibility of the hydrophobic fluorophores. The polymer is designed to self-assemble to form nanoparticles with high loading capabilities due to the presence of pendant phenyl groups in the hydrophobic portion of the polymer, allowing for increased π–π interactions with the fluorophores.[54] The copolymer (PhPCL-PEG) was synthesized using ring-opening polymerization (ROP) and was characterized using NMR and GPC techniques. Full synthetic details and NMR spectra can be found in the ESI,‡ Schemes S1–S3 and Fig. S1–S11.

Spectroscopic analysis

Unencapsulated fluorophores. All three derivatives exhibited absorbance maxima in the NIR-I region (Fig. 2, solid lines), with **DMA-TTDT$_2$** having the furthest red-shifted value of λ_{max}^{abs} = 736 nm. **Pip-TTDT$_2$** and **Morp-TTDT$_2$** possessed absorbance maxima of 726 and 710 nm, respectively.

The broad absorption bands are indicative of the ICT nature, which results in the narrow HOMO–LUMO gaps for the fluorophores.[55] The optical HOMO–LUMO gaps (E_g^{opt}) were measured to be 1.68 eV for **DMA-TTDT$_2$**, 1.70 eV for **Pip-TTDT2**, and 1.74 eV for **Morp-TTDT$_2$**.[56] Molar absorption coefficients (ε) for the three fluorophores ranged from 15 000 M^{-1} cm^{-1} for **Pip-TTDT$_2$** to 20 000 M^{-1} cm^{-1} for **Morp-TTDT$_2$**. The ε value for **DMA-TTDT$_2$** fell in between, as a value of 17 000 M^{-1} cm^{-1} was calculated. Remarkably, these values are similar to what is observed for the current leading D–A–D-based fluorophores, (*i.e.*, BBTD).[57] Each of the three fluorophores was hypothesized to be sensitive to increasing acidity as a result of the alkyl amine donors being used. To measure this, we made solutions of each fluorophore dissolved in 6 mL of acetone and 1 mL of H$_2$O at pH 7, 5, and 3 (Fig. S12–S14 and Table S1, ESI‡).

Fig. 2 Normalized absorbance (solid lines) and emisison (dashed lines) spectra of the TTDT$_s$ based fluorophores in 10^{-5} M CHCl$_3$.

For **DMA-TTDT$_2$**, upon decreasing from pH 7 > pH 5 > pH 3, there was gradual bathochromic shift in the λ_{max}^{abs} from 725 to 729 nm. Interestingly, the highest absorbance intensity was seen at pH 3 for **DMA-TTDT$_2$**. Under increasingly acidic conditions, the λ_{max}^{abs} for **Pip-TTDT$_2$** was found to blue-shift significantly from 716 nm at pH 7 to 714 nm at pH 5 to 698 nm at pH 3 with corresponding hypochromic shifts in the absorbance intensity at the lowest pH values. There was not a noticeable change in the λ_{max}^{abs} for **Morp-TTDT$_2$** under acidic conditions. There was a 1 nm shift from 704 nm to 703 nm at pH 7 to pH 5 and 3. However, there was a slight decrease in the absorbance intensity at pH 3, compared to pH 7 and 5.

The emission maxima (λ_{max}^{emi}) for the three fluorophores ranged from 1030 nm for **Pip-TTDT$_2$** to 1075 nm for **DMA-TTDT$_2$**, with **Morp-TTDT$_2$** having an λ_{max}^{emi} = 1060 nm (Fig. 2, dashed lines). The emission band shape and broadness of the derivatives are found to mirror their corresponding absorbance band profiles. The Stokes shifts of the three fluorophores were all quite large, with measured values exceeding 300 nm. This is another characteristic feature of compounds that exhibit ICT properties.[58] The relative fluorescence quantum yield (Φ) measurements were made utilizing IR-1061 as the reference fluorophore in CHCl$_3$. **Morp-TTDT$_2$** was seen to have the highest QY value of 0.057% followed by **Pip-TTDT$_2$** (0.043%) and **DMA-TTDT$_2$** (0.034%). The QYs of the three fluorophores are comparable to other reported NIR-II D–A–D derivatives and commercial fluorophores.[19]

Transient absorption (TA) measurements were performed to study the excited state dynamics of the unencapsulated dyes in chloroform solution. The TA spectra at varying time delays as well as single wavelength kinetics are presented in Fig. S20(a)–S23(a) (ESI‡). Similar excited state dynamics are seen for all dyes. Photoexcitation at the blue edge of λ_{max}^{abs} (650 nm for all dyes) yields formation of an excited state absorption (ESA) with two peaks: a higher energy peak centered at approximately 485 nm and broad, lower energy peak centered at approximately 550 nm. Additionally, photoinduced transparencies (ground state bleach, GSB) form in two regions: <450 nm and >650 nm. These GSB regions are partially obscured by the high energy cut off of the probe spectrum and the low energy laser scatter, respectively.

Single wavelength kinetics were taken at the absorption maximum of the ESA (550 nm) to extract excited-state lifetimes for the unencapsulated dye species. These kinetics fit well with single-exponential decay functions. Due to the emissive properties of these dyes, this indicates that the primary relaxation seen in the TA experiments is through photon emission, with minimal contribution from solvent rearrangement or nuclear motion. These lifetimes indicate that the three fluorophores are overall short lived, with **Pip-TTDT$_2$** having the longest lifetime value of 105 ps, followed by **Morp-TTDT$_2$** and **DMA-TTDT$_2$**, having values of 63.5 and 53.0 ps, respectively.

Theoretical (CAM-B3LYP) calculations of absorption and emission spectra are reported in the ESI.‡ S$_0$ and S$_1$ geometries of the compounds were optimized using the CAM-B3LYP density functional with the cc-pVDZ basis set. The NTOs for
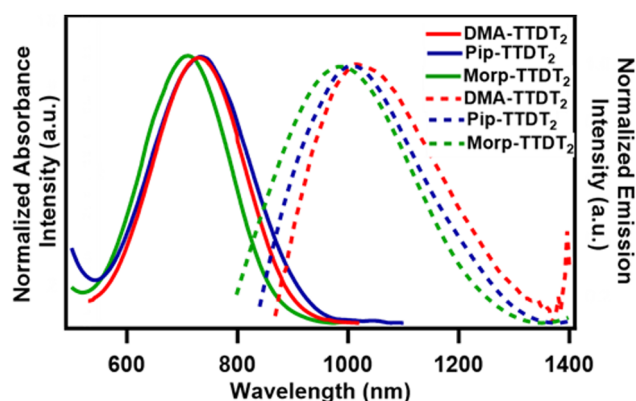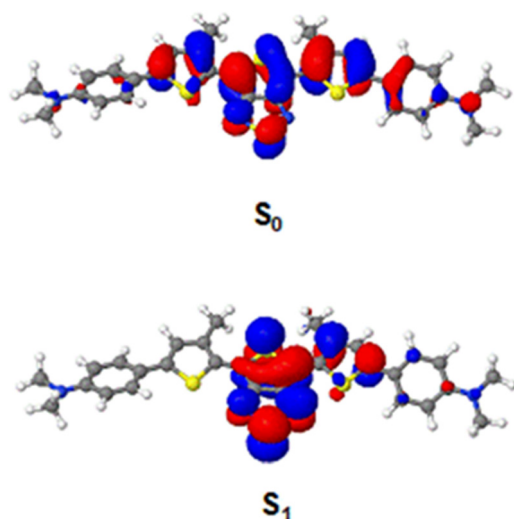
Fig. 3 Ground (S0) and excited (S1) state natural transition orbitals (NTOs) for DMA-TTDT2. The corresponding oscillator strength is 0.62, NTOs were computed using CAM-B3LYP with the cc-pVDZ basis set for the hydrogen and carbon atoms and aug-cc-pVDZ for the remaining elements.

Fig. 4 Normalized absorbance (solid lines) and emission (dashed lines) spectra of the encapsulated fluorophores in 1 mg mL^{-1} of H$_2$O.

DMA-TTDT$_2$ can be seen in Fig. 3 while those for **Pip-TTDT$_2$** and **Morp-TTDT$_2$** can be found in the ESI.‡ The computed absorption maxima are in good agreement with experimental results showing a slight overestimation of absorption energies by ∼15–30 nm. The computed results aid to support TA measurements as the ESA can be assigned to the absorption of the reduced TTDT$_2$ core based upon the calculated S$_1$ NTO. Photoexcitation into the S$_1$ transition yields a formal charge transfer from the donor substituents into the acceptor core. The GSB regions correspond to the inverted absorption spectra of the oxidized donor substituents. Visual observation shows a similar decay for both the ESA and GSB regions, indicating that the TA measurements are tracking the decay of a one-level system back into the ground state.

The simulations of emission spectra yield significantly underestimated energies of emission maxima (by 215–250 nm) and Stokes shift as a result. The discrepancies in theory for emission calculations can be attributed to the approximations in TDDFT, which errors become particularly significant away from the equilibrium ground-state geometries.[59]

Fluorophore–polymer nanoparticles

Upon encapsulation and solvation, the λ_{max}^{abs} for both **Pip-TTDT$_2$** and **Morp-TTDT$_2$** were found to have red-shifted to 734 and 721 nm, respectively (Fig. 4, solid lines). The absorbance maxima for the encapsulated **DMA-TTDT$_2$** was seen to have blue-shifted to 720 nm. The E_g^{opt} for the encapsulated fluorophores were subsequently still small, ranging from 1.69 eV to 1.72 eV.

To measure the pH sensitivity of the encapsulated fluorophores, we added 1 mL of a 1 mg mL^{-1} nanoparticle solution to 1 mL of the corresponding pH solution. We observed similar trends to the acetone/H$_2$O pH study in that the λ_{max}^{abs} for the
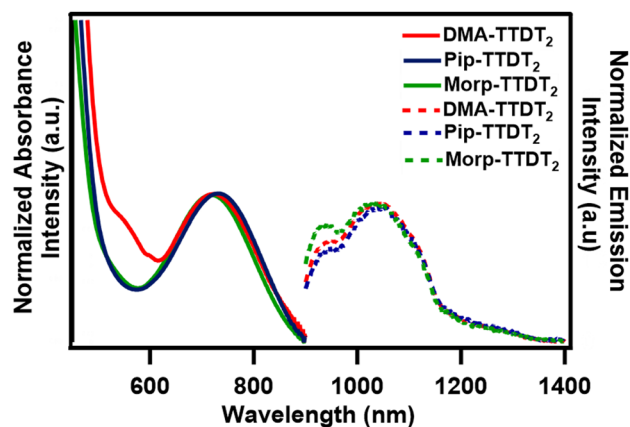
encapsulated **DMA-TTDT$_2$** was red-shifted upon increasing acidity. At pH 7, pH 5, and pH 3, the λ_{max}^{abs} were found to be 720, 729, and 740 nm, along with a decrease in the absorbance intensity at each pH. The λ_{max}^{abs} of the encapsulated **Pip-TTDT$_2$** was also seen to blue-shift as pH was decreased. An λ_{max}^{abs} of 734 nm was observed at pH 7 followed by 731 nm and 728 nm at pH 5 and 3, respectively. Similar to the encapsulated **DMA-TTDT$_2$**, there were also hypochromic shifts in absorbance intensity for the encapsulated **Pip-TTDT$_2$** as acidity increased. There were more changes in the absorbance properties for the encapsulated **Morp-TTDT$_2$** than what was seen in the acetone/H$_2$O study. Greater hypsochromic shifts when pH was decreased from pH 7 > pH 5 > pH 3 were observed as λ_{max}^{abs} of 721, 714, and 713 nm were recorded. Likewise, decreases in absorbance intensity were seen as pH was lowered for the encapsulated **Morp-TTDT$_2$**. Tabulated absorbance values and absorbance spectra for the pH studies can be found in the ESI,‡ Table S1 and Fig. S15–S19.

We observed interesting changes in the emissive properties for the encapsulated fluorophores (Fig. 4, dashed lines). Hypsochromic shifts in the λ_{max}^{emi} were seen for both the encapsulated **DMA-TTDT$_2$** (1036 nm) and **Morp-TTDT$_2$** (1024 nm) while a red-shift in the λ_{max}^{emi} was observed for **Pip-TTDT$_2$** (1042 nm) when compared to the free dyes. Each of the encapsulated fluorophores still presented Stokes shifts greater than 300 nm. Fluorescence QY values were seen to increase by approximately one order of magnitude for the encapsulated fluorophores, which is an attractive property for fluorescence bioimaging applications. The most significant increase was observed for encapsulated **DMA-TTDT$_2$**, with a QY value of 0.28% being measured, while QY values for **Pip-TTDT$_2$** and **Morp-TTDT$_2$** increased to 0.18% and 0.13%, respectively. Along with increases in QY for the encapsulated fluorophores, their excited state lifetimes were also found to be extended.

TA measurements performed on the encapsulated species (Fig. S20(a)–S23(a), ESI‡) show similar excited state dynamics to the unencapsulated dyes. The ESA for all encapsulated dyes, however, does not show the same 485 nm peak as seen in their

4374 | *J. Mater. Chem. C*, 2024, **12**, 4369–4383

This journal is © The Royal Society of Chemistry 2024

unencapsulated counterparts. This is attributed to broadening of the lower energy feature (approximately 550 nm) due to interaction with the encapsulating polymer. Single-wavelength kinetics fit well with biexponential decay functions, indicating that, while these measurements are still observing a two level system, there are increased interactions with the fluorophore–polymer network, causing a new energy decay pathway in addition to photon emission. Within the polymer encapsulation, excited state lifetimes are extended relative to their unencapsulated counterparts.

Encapsulated **DMA-TTDT₂** and **Morp-TTDT₂** saw increases to 153 ps and 205 ps, with the largest increase being observed with the encapsulated **Pip-TTDT₂** as a lifetime value of >8 ns was measured. Although increases in the excited state lifetimes are commonly observed when analyzing encapsulated fluorophores *versus* free fluorophores, the large increase seen for the encapsulated **Pip-TTDT₂** is a result of increased fluorophore–polymer interactions affording a larger amount of the dye uptaken into each nanoparticle.[60,61] This increased uptake relative to the other fluorophores affords an increase in delocalization of the excited state due to molecular aggregation.[60–62] TAS spectra for the free and encapsulated derivatives can be found in the ESI,‡ Fig. S20–S23.

Nanoparticle morphology

DLS and TEM techniques were utilized to characterize the morphological properties of the encapsulated fluorophores. The nanoparticle solutions were formulated using the thin-film technique. DLS measurements for the encapsulated fluorophores provided nanoparticle sizes ranging from 51.8 nm for the encapsulated **DMA-TTDT₂** to 83.9 nm for the encapsulated **Pip-TTDT₂**. The **Morp-TTDT₂** nanoparticles had sizes between the two, with an average hydrodynamic radius of 61.9 nm. The polydispersity index (PDI) for the encapsulated fluorophores ranged from 0.122 for **DMA-TTDT₂** to 0.172 for **Morp-TTDT₂** to 0.218 for **Pip-TTDT₂**. The PDI values indicate that the encapsulated fluorophore nanoparticle solutions are not as monodisperse as desired, as monodispersity would be indicated with PDI values near 0.1.[63] The empty polymer nanoparticles were seen to have sizes of 124.5 nm *via* DLS with a PDI value of 0.320. The difference in nanoparticle sizes for the encapsulated fluorophores when compared to the empty polymer nanoparticles, along with the corresponding color of the nanoparticle solutions (Fig. S24, ESI‡), is indicative of successful encapsulation of the fluorophores. The nanoparticle sizes obtained from TEM validate the sizes obtained from DLS. **DMA-TTDT₂** nanoparticles possessed the smallest average size of 48.1 ± 14 nm, followed by **Morp-TTDT₂** nanoparticles (73.5 ± 22 nm) and the **Pip-TTDT₂** nanoparticles (84.4 ± 23 nm). The empty polymer nanoparticles were found to have an average size of 90.8 ± 23 nm *via* TEM. TEM images of the three encapsulated fluorophores along with the empty polymer nanoparticles can be seen in Fig. 5. Encapsulation efficiencies (EE) ranged from 15.0% for encapsulated **Morp-TTDT₂** and **DMA-TTDT₂** to 23.0% for **Pip-TTDT₂**. Tabulated nanoparticle size
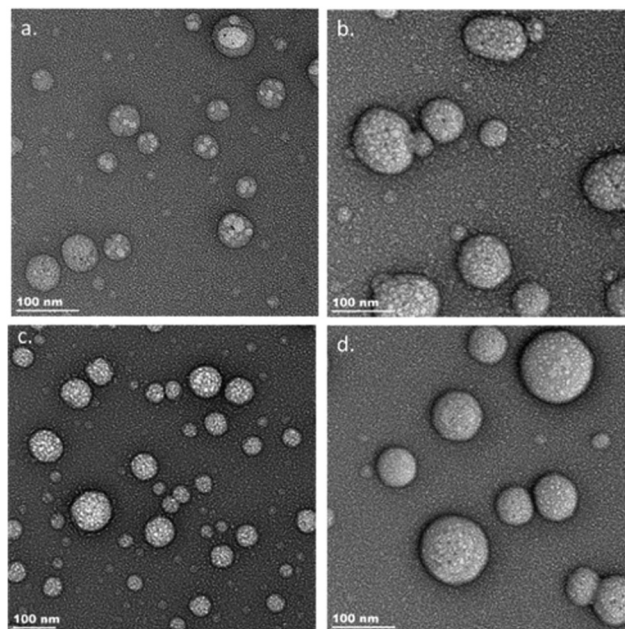

Fig. 5 TEM images of encapsulated **DMA-TTDT₂** (a) **Morp-TTDT₂** (b) **Pip-TTDT₂** (c) and empty PhPCL-PEG (d).

data and DLS spectra can be found in the ESI,‡ Table S2 and Fig. S25–S32.

Photothermal efficiency

Photothermal efficiency (η) experiments were performed to understand the potential use of the encapsulated fluorophores as photothermal therapy (PTT) agents. Analysis of the molar absorptivity and QY values indicated that the fluorophores were efficient at absorbing radiation but relatively inefficient at emitting the absorbed photons. This is a consequence of the low energy band gaps, however, it is indicative of photothermal properties in which absorbed photons are converted to heat.[64] For strictly bioimaging purposes, non-radiative energy loss is considered detrimental, however, our measured QY values are within a clinically relevant range, and as such, the observed photothermal effect can be a valuable tool.

Encapsulated **DMA-TTDT₂** was shown to have the highest average η value (62 ± 5%) of the encapsulated fluorophores. **Pip-TTDT₂** and **Morp-TTDT₂** nanoparticles exhibited similar η values, with measured average photothermal efficiencies of 46 ± 5% and 47.0 ± 1.4%, respectively. Using an 808 nm laser with 0.4 W cm⁻² the **Pip-TTDT₂** nanoparticles showed the lowest average change in temperature ($\Delta T = 6.59\ °$C), while the **DMA-TTDT₂** and **Morp-TTDT₂** nanoparticles had $\Delta T = 7.27\ °$C and $\Delta T = 8.25\ °$C, respectively. The temperature change increased when higher power was used, but significant degradation was observed for **Morp-TTDT₂** at this power (Fig. S33(b), ESI‡). The photothermal efficiencies of the encapsulated fluorophores are much greater than values obtained for commonly studied PTT agents, such as single-walled carbon nanotubes (SWCNTs, 38.3%).[65,66] These initial results indicate that each encapsulated fluorophore, in addition to their NIR-II emission

This journal is © The Royal Society of Chemistry 2024

J. Mater. Chem. C, 2024, **12**, 4369–4383 | **4375**

properties, represents applicable theranostic capabilities. Detailed photothermal data can be found in the ESI,‡ Fig. S33–S41.

Cytotoxicity and hemobiocompatibility

Comparative cytotoxicity of non-encapsulated (empty polymer nanoparticle) and the three encapsulated fluorophores were assessed with a CellTiter-Glo luminescent assay using MDA-MB-231 (TNBC cell line) and MCF-10A cells (non-tumorigenic) (Fig. 6(a) and (b)). Here, the method affords the determination of live cells based on the ATP quantitation after exposing the cells to seven different nanoparticle concentrations for 24 h. Within the tested concentrations, no significant toxicity (cell viability $> 80\%$) was observed relative to a positive (nanoparticles) and negative control (untreated cells).
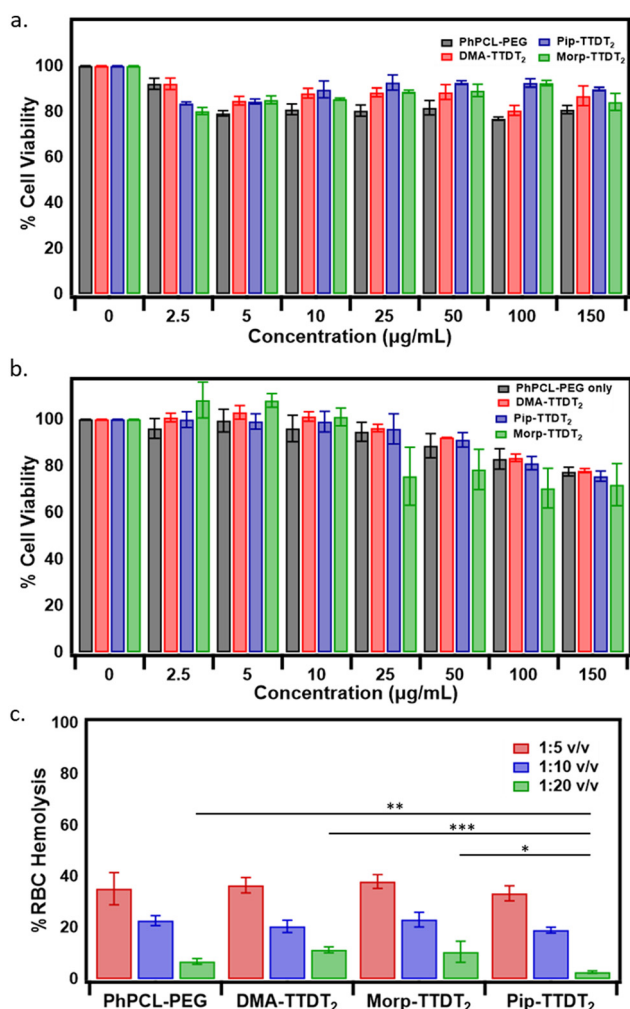

Fig. 6 Cell viability results for MDA-MB-231 (a) and MCF-10A cells (b) are expressed as percent viability and present as mean ± standard deviation of 3 independent experiments ($n = 3$). Hemolysis assay on mouse red blood cells at 125 μg mL^{-1} concentration. The 1:20, 1:10, and 1:5 dilutions are 0.05, 0.1, and 0.2 mg mL^{-1} respectively. Average % RBC hemolysis in response to nanoparticles *ex vivo* with standard error of the mean (SEM) ($n = 4$) (c).

To gauge the biocompatibility profile of the empty, **DMA-TTDT$_2$**, **Morp-TTDT$_2$**, and **Pip-TTDT$_2$** nanoparticles with blood cells in systemic circulation after intravenous injection, red blood cell (RBC) hemolysis was measured. We assessed the three fluorophores encapsulated in PhPCL-PEG nanoparticles and the empty nanoparticles with BALB/c mouse RBCs at a nanoparticle dosage range of 0.05, 1.0, and 2.0 mg mL^{-1}.[47–49] Interestingly, the highest end of this nanoparticle treatment concentration range (1:5 v/v, or 0.2 mg mL^{-1}) shows the highest overall hemolytic activity, averaging at 35.8 ± 2.0% across all samples tested (ANOVA; $p = 0.45$) (Fig. 6(c)). In comparison, the hemolytic activity of all samples decreased in proportion with decreasing nanoparticle-treatment concentration (1:10 v/v, or 0.1 mg mL^{-1} averaging at 21.4 ± 1.9%, ANOVA $p = 0.06$), with the lowest end of the nanoparticle treatment concentration range (1:20 v/v, or 0.05 mg mL^{-1}) showing the highest biocompatibility across all samples tested, along with the most deviation between samples (averaging at 7.9 ± 4.0%, ANOVA $p = 0.0005$).

Notably, **Pip-TTDT$_2$** nanoparticles consistently exhibited the lowest, but non-significant, hemolytic response among the three encapsulated fluorophores at the 0.2 and 0.1 mg mL^{-1} treatment concentration ranges. However, **Pip-TTDT$_2$** nanoparticles demonstrated the most negligible levels of hemolysis at 0.05 mg mL^{-1} (2.7 ± 0.46%) was significantly lower than the empty **PhPCL-PEG** nanoparticles ($p = 0.005$), **DMA-TTDT$_2$** nanoparticles ($p = 0.0004$), and **Morp-TTDT$_2$** nanoparticles ($p = 0.03$) at this lowest treatment concentration. This suggests that the variance in nanoparticles effect on RBC hemolysis is derived not from free fluorophore but rather a result of molecular arrangement and structural conformation between the polymer and each NIR-II dye. In all, the encapsulated fluorophores show excellent biocompatibility with mammary cells at all concentrations and acceptable hemocompatibility at a dosage of 1:20 v/v.

Discussion

Analyzing the λ_{max}^{abs} for each of the fluorophores, the low-energy transitions are predominantly attributed to the ICT nature of the D–A–D architecture.[67] In the design of the fluorophores, we chose to utilize the alkyl amine donors as they are more effective in their contributions to the electronic structure, specifically to the HOMO, when compared to aryl amine donors.[28,68] The natural transition orbitals (NTO) diagrams, reported in ESI‡ (Fig. S42), reveal that excitation from the ground-state (S$_0$) to the excited state (S$_1$) involves the transfer of electron density primarily from thiophene spacers to the acceptor with minor contributions from the amine donors themselves. However, when comparing the experimental absorbance properties of **DMA-TTDT$_2$**, **Morp-TTDT$_2$**, and **Pip-TTDT$_2$** to previous TTD-based fluorophores with aryl amine donors, there are noticeable bathochromic shifts that indicate the alkyl amine donors do positively affect the optical properties.[27] The narrow energy gaps can also be attributed to an increase in

4376 | *J. Mater. Chem. C*, 2024, **12**, 4369–4383

This journal is © The Royal Society of Chemistry 2024

planarity due to the relatively small size of the peripheral amine donors. The DFT-computed ground state dihedral angles between the thiophene spacers and the amine donors (θ_2 and θ_3, Table S3, ESI‡) are found to deviate $\sim$23–24° from the conjugated backbone. In the excited state, however, much smaller dihedral angles between the spacer and donor moieties are observed (Table S3, ESI‡). This effectively extends the overall conjugation of the fluorophores, which is a known method to result in red-shifted absorbance properties.[69] Additionally, TTD-based compounds have been shown to possess radical species *via* computational and experimental results.[27,70] The presence of these radical species can also result in low-energy excitations and are hypothesized to occur to relieve the hypervalent strain on the sulfur atom in the thiadiazole ring.[71] We observed a low-intensity signal at 336 mT ($g = 2.006$) for each of the three fluorophores through EPR experiments, indicating the presence of unpaired electrons (Fig. S43, ESI‡). Although the radical species can affect the photophysical characteristics of the fluorophores, namely the absorbance properties, the measured spin state concentrations were found to be negligible ($<10\%$). The lack of contributions of the radical species dictates that the photophysical properties of the fluorophores are primarily a result of ICT processes. For the encapsulated fluorophores, the minor shifts in the λ_{max}^{abs} are expected to occur due to changing the environment around the fluorophore. We attribute these shifts to different packing arrangements of the fluorophores inside the hydrophobic portion of the nanoparticle.[72]

We initially hypothesized that the observed changes in the absorbance properties of the fluorophores at varying pH values would be a result of the protonation of the peripheral nitrogen atoms on the donors. However, the computational calculations (Table S4, ESI‡) on the basicity of all the nitrogen atoms in the fluorophore confirm that the sp^2-hybridized nitrogen atoms comprising the thiadiazole ring are slightly more basic than those that comprise the donor units. As such, we can only speculate that protonation occurs at the acceptor nitrogens, leading to variations in the optical properties. For both free and encapsulated **DMA-TTDT₂**, the bathochromic shift in the λ_{max}^{abs} are speculated to be a result of the preferential protonation of the nitrogen atoms on the TTD core, effectively increasing the electron-deficient nature of the acceptor. Contrarily, the basicity of the nitrogen atoms in the donor for **Pip-TTDT₂** is much

closer to that of the nitrogen atoms in the acceptor. This may result in protonation occurring at both the donor and acceptor nitrogen atoms, resulting in a blue-shifted λ_{max}^{abs} for both the encapsulated and free fluorophore. For **Morp-TTDT₂**, the basicity of the donor nitrogen atoms falls in between the values calculated for **DMA-TTDT₂** and **Pip-TTDT₂**. Likewise, the observed changes are not as drastic as those observed for the other two derivatives, as evident by the minuscule changes observed in the acetone/H₂O study. The greatest change in λ_{max}^{abs} was observed for the encapsulated **Morp-TTDT₂** as the acidity was increased from pH 7 to 5, and upon changing to pH 3, only a 8 nm blue-shift was seen. This could be due to the presence of the oxygen atom in the donor ring stabilizing the protonated nitrogen atom in the donor. It is, however, important to note that pH-sensitivity is nominal with variations in λ_{max}^{abs} being $\leq$20 nm. Additionally, we studied the effects of pH on the core of the molecule without the amine donors (Scheme S1, compound 3, ESI‡) under the same conditions. No prominent changes were observed in the absorbance spectra in either the acetone/H₂O or for the encapsulated core upon variation in pH (Fig. S18 and S19, ESI‡).

The NIR-II emission properties of the three fluorophores are predominantly attributed to the ICT processes that occur, resulting in narrow optical gaps.[73] We conclude that the alkyl amine donors do affect the electronic properties of the fluorophores to a greater degree than what is indicated by the absorbance experiments.[74] This is also confirmed upon comparison to our previously synthesized TTD-based fluorophores that utilized an aryl amine carbazole as the donor.[27] We attribute the large Stokes shift values to the changes in bond length between the ground- and excited-state structures.[50] Electron-transfer processes between the alkyl amine donors and the TTD acceptor result in either the shortening and elongation of the specified carbon–carbon bonds as indicated by computational results (Table S5, ESI‡). The QY values of the three free fluorophores are comparable to other D–A–D NIR-II emissive materials (Table 1).[75] A photophysical phenomenon known as the energy-gap law is commonly used to describe these low QY values, essentially stating that along with decreasing optical gaps, there will be an increase in non-radiative relaxations between electronic states detracting from the desired radiative processes.[76,77] The short-lived excited-state lifetimes of the derivatives are hypothesized to result from fast

Table 1 Photophysical data of TTDT₂ derivatives in solution (CHCl₃) and encapsulated in PhPCL-PEG nanoparticles (H₂O)

	λ_{max}^{abs} [nm (eV)]	λ_{max}^{emi} [nm (eV)]	Stokes shift [nm (eV)]	ε ($\times 10^4$ M^{-1} cm^{-1})	LT^c (ps)	QY (%)
Solution^a						
DMA-TTDT₂	736 (1.68)	1075 (1.15)	339 (0.53)	1.7	53.0	0.034
Pip-TTDT₂	726 (1.70)	1030 (1.20)	304 (0.50)	1.5	105	0.043
Morp-TTDT₂	710 (1.74)	1060 (1.17)	350 (0.57)	2.0	63.5	0.057
Nanoparticles^b						
DMA-TTDT₂	720 (1.72)	1036 (1.19)	316 (0.52)	—	153	0.28
Pip-TTDT₂	734 (1.69)	1042 (1.18)	308 (0.49)	—	<8000	0.18
Morp-TTDT₂	721 (1.72)	1024 (1.21)	303 (0.50)	—	205	0.13

^{a} Indicates studies performed in 10^{-5} M CHCl₃. ^{b} Indicates studies performed with 1 mg mL^{-1} nanoparticle (aqueous) solutions. ^{c} Lifetime (LT) values presented are a result of overall excited state LT measurements.

This journal is © The Royal Society of Chemistry 2024

J. Mater. Chem. C, 2024, **12**, 4369–4383 | **4377**

reorganization and subsequent relaxation of the excited-state structure back to the ground-state structure.[78]

The encapsulated fluorophores exhibited slight changes in the λ_{max}^{emi} when compared to the free dyes in solution (Table 1). We can attribute these shifts to the aggregation patterns, similar to what was described for the changes in the λ_{max}^{abs}. The most interesting changes that were observed were the increase in QY and excited-state lifetime values. Generally, the increase in QY values for the encapsulated fluorophores is attributed to the presence of the pendant-phenyl groups in the hydrophobic portion of the polymer. These groups can prevent undesirable intermolecular interactions that can result in emission quenching.[79] Additionally, the environment provided by the hydrophobic core of the polymer nanoparticle is nonpolar and may also contribute to a decrease in the ICT effect.[80,81]

Interestingly, within the series **DMA-TTDT₂** exhibited the largest increase in QY upon encapsulation. For free **DMA-TTDT₂**, there is a large difference in the ground and excited state dihedral angles between the thiophene spacers and the acceptor (Table S3, ESI‡). We speculate that upon relaxation, more energy is required to reorganize from the excited state species back to the ground state species and this is detrimental to the QY for free **DMA-TTDT₂**. Therefore, upon encapsulation into an aggregate environment, the rotational freedom between the thiophene spacers and the acceptor is less pronounced and subsequently an increase in QY is observed for encapsulated **DMA-TTDT₂**. Additionally, the increase in the excited-state lifetime values for the encapsulated fluorophores is a result of the stabilization of the excited-state species.[60,62]

DLS analysis of the nanoparticle solutions shows a range of sizes for each of the encapsulated fluorophores. The observed nanoparticle sizes can be attributed to the differing sizes of the alkyl amine donor units along with the differences in EE values (*vide infra*). The PDI obtained by DLS showed that the nanoparticle solutions were not monodispersed, as PDI values greater than 0.1 were found for the encapsulated fluorophore nanoparticles as well as the empty polymer nanoparticles. The variation of nanoparticle sizes obtained from DLS is confirmed upon analysis of the corresponding TEM images. This can be directly correlated to the polydispersity observed with the empty polymer nanoparticles. Upon encapsulation of the fluorophores, the smaller nanoparticle sizes relative to the empty polymer nanoparticles indicate tight intermolecular interactions within the hydrophobic portion of the nanoparticle. The lower EE values (15% and 23%) for the nanoparticles presumably result from the preferred intermolecular interactions between the fluorophores rather than the intermolecular interactions between the fluorophores and the PhPCL-PEG polymer.[82] Importantly, however, these nanoparticle sizes are still within the range of what is appropriate for practical applications (10–200 nm).[83,84]

The photothermal properties of the three encapsulated fluorophores are a result of the non-radiative energy loss of the fluorophores. For strictly fluorescence bioimaging purposes, non-radiative energy loss is not a desirable property as

that results in decreased brightness of the emissive species. However, the measured QY values of the encapsulated fluorophores are similar to other NIR-II emissive fluorophores that are promising compounds for fluorescence bioimaging.[19] As such, the measured photothermal properties indicate the potential of these compounds to be used in a theranostic setting (Fig. S33–S41, ESI‡). Encapsulated **DMA-TTDT₂** was seen to have the highest photothermal efficiency value. It is reported that fluorophores that utilize alkyl amines as electron-donors tend to show higher non-radiative decay rates.[85] This results from the preference for the amine substituent twisting out of plane to adopt a lower-energy ground state structure resembling a twist-induced charge transfer (TICT) geometry. The dimethyl aniline donor used in **DMA-TTDT₂** is well-known for its ability to take on a TICT structure and that is illustrated by it possessing the largest η value.[86,87] The photothermal efficiencies of **Pip-TTDT₂** and **Morp-TTDT₂** were similar, which is to be expected due to the structural similarities of the amine substituent. The decrease in η values for the **Pip-TTDT₂** and **Morp-TTDT₂** nanoparticles when compared to **DMA-TTDT₂** is a result of the rigidification of the cyclic amine substituents as they cannot rotate as freely as their dimethyl amine counterpart.[88]

Considering the application of our fluorophores for biomedical research, the putative therapeutic potential of the encapsulated fluorophores was evaluated. Comparative cytotoxicity using cancerous (MDA-MB-231) and healthy human mammary cells (MCF-10A) did not indicate significant toxicity. However, a noticeable and undesirably elevated level of apoptosis is observed for MCF10A at concentrations above traditional dosing amounts (5–35 μg mL⁻¹).[89] Polymer aggregation at higher concentrations is a common underlying cause of cytotoxic response for nanoparticle based therapies; however, MDA-MB-231 displayed comparative insensitivity to varying concentrations.[90,91]

Additionally, RBC hemolysis results demonstrate an acceptable dosing threshold for hemocompatibility, with the least RBC lysis at 1:20 v/v (0.05 mg mL⁻¹) and a significant difference between the low hemolytic potential of **Pip-TTDT₂** compared to **Morp-TTDT₂**, **DMA-TTDT₂**, and empty PhPCL-PEG carrier at the lowest treatment concentration. These results suggest that the physicochemical properties of the polymeric carrier, as well as polymeric molecular nanoassembly and structural conformation with each NIR-II dye, may direct the cellular toxicity profile as well as biological and therapeutic interactions *in vivo* after administration, albeit more studies are needed to verify this proposed hypothesis.

Conclusions

We have successfully synthesized a series of TTD-based fluorophores possessing NIR-II emissive properties, in addition to having pH sensitivity and photothermal capabilities. By employing alkyl amine donor substituents, we were able to manipulate the structural and electronic properties of the

4378 | *J. Mater. Chem. C*, 2024, **12**, 4369–4383

This journal is © The Royal Society of Chemistry 2024

fluorophores, enabling these low-energy excitations to occur. Spectroscopic characterization of the three fluorophores in CHCl$_3$ shows that the fluorophores have λ_{max}^{abs} ranging from 710 to 736 nm with large Stokes shifts, as the λ_{max}^{emi} are found to range from 1030 to 1075 nm. Theoretical calculations reveal the intramolecular charge transfer character of the absorption peaks. Upon encapsulation, slight shifts are observed in the absorbance and emission maxima, but importantly, we see increases in the fluorescence QY compared to the free fluorophores. The initial pH studies of the compounds provided insight into the potential biosensing applications of the fluorophores, although further study is needed to highlight their efficacy in such applications. The photothermal properties of the fluorophores are perhaps the most interesting detailed, as compounds that can generate heat are being implemented in the treatment of various types of cancers.[92] The highest photothermal efficiency value was found to be 62.0% for **DMA-TTDT$_2$** nanoparticles, which is comparable to commercial agents. Additionally, no considerable cytotoxicity is observed at ideal dosing concentrations with human mammary cells, and acceptable hemocompatibility is demonstrated at 1 : 20 v/v doses (0.05 mg mL^{-1}). Further study is needed to validate how the photophysical, pH, and photothermal properties translate to *in vitro* and *in vivo* applications. These initial results are exciting, providing a novel series of biocompatible organic fluorophores for potential use as theranostic agents.

Author contributions

The manuscript was written through the contributions of all authors. All authors have given approval to the final version of the manuscript.

Conflicts of interest

There are no conflicts to declare.

Acknowledgements

Notes and references

1   F. Ding, Y. Zhan, X. Lu and Y. Sun, Recent Advances in Near-Infrared II Fluorophores for Multifunctional Biomedical Imaging, *Chem. Sci.*, 2018, **9**(19), 4370–4380, DOI: **10.1039/C8SC01153B**.

2   Z. Chen, D.-D. Deng, R. Aav, V. Borovkov and Y. Sun, Editorial: Stimuli-Responsive Emissive Organic and Metal–Organic Compounds, *Front. Chem.*, 2022, **10**, 946617, DOI: **10.3389/fchem.2022.946617**.

3   G. Huang, Q. Xia, W. Huang, J. Tian, Z. He, B. S. Li and B. Z. Tang, Multiple Anti-Counterfeiting Guarantees from a Simple Tetraphenylethylene Derivative – High-Contrasted and Multi-State Mechanochromism and Photochromism, *Angew. Chem.*, 2019, **131**(49), 17978–17983, DOI: **10.1002/ange.201910530**.

4   M. Gao, F. Yu, C. Lv, J. Choo and L. Chen, Fluorescent Chemical Probes for Accurate Tumor Diagnosis and Targeting Therapy, *Chem. Soc. Rev.*, 2017, **46**(8), 2237–2271, DOI: **10.1039/C6CS00908E**.

5   L. van Manen, H. J. M. Handgraaf, M. Diana, J. Dijkstra, T. Ishizawa, A. L. Vahrmeijer and J. S. D. Mieog, A Practical Guide for the Use of Indocyanine Green and Methylene Blue in Fluorescence-Guided Abdominal Surgery, *J. Surg. Oncol.*, 2018, **118**(2), 283–300, DOI: **10.1002/jso.25105**.

6   Y. Li, Y. Liu, Q. Li, X. Zeng, T. Tian, W. Zhou, Y. Cui, X. Wang, X. Cheng, Q. Ding, X. Wang, J. Wu, H. Deng, Y. Li, X. Meng, Z. Deng, X. Hong and Y. Xiao, Novel NIR-II Organic Fluorophores for Bioimaging beyond 1550 Nm, *Chem. Sci.*, 2020, **11**(10), 2621–2626, DOI: **10.1039/C9SC06567A**.

7   A. L. Antaris, H. Chen, K. Cheng, Y. Sun, G. Hong, C. Qu, S. Diao, Z. Deng, X. Hu, B. Zhang, X. Zhang, O. K. Yaghi, Z. R. Alamparambil, X. Hong, Z. Cheng and H. Dai, A Small-Molecule Dye for NIR-II Imaging, *Nat. Mater.*, 2016, **15**(2), 235–242, DOI: **10.1038/nmat4476**.

8   J. Wu, Z. Shi, L. Zhu, J. Li, X. Han, M. Xu, S. Hao, Y. Fan, T. Shao, H. Bai, B. Peng, W. Hu, X. Liu, C. Yao, L. Li and W. Huang, The Design and Bioimaging Applications of NIR Fluorescent Organic Dyes with High Brightness, *Adv. Opt. Mater.*, 2022, **10**(8), 2102514, DOI: **10.1002/adom.202102514**.

9   G. Hong, S. Diao, A. L. Antaris and H. Dai, Carbon Nanomaterials for Biological Imaging and Nanomedicinal Therapy, *Chem. Rev.*, 2015, **115**(19), 10816–10906, DOI: **10.1021/acs.chemrev.5b00008**.

10 Q. Shen, S. Wang, N.-D. Yang, C. Zhang, Q. Wu and C. Yu, Recent Development of Small-Molecule Organic Fluorophores for Multifunctional Bioimaging in the Second near-Infrared Window, *J. Lumin.*, 2020, **225**, 117338, DOI: **10.1016/j.jlumin.2020.117338**.

11 G. Hong, J. C. Lee, J. T. Robinson, U. Raaz, L. Xie, N. F. Huang, J. P. Cooke and H. Dai, Multifunctional *in Vivo* Vascular Imaging Using Near-Infrared II Fluorescence, *Nat. Med.*, 2012, **18**(12), 1841–1846, DOI: **10.1038/nm.2995**.

12 G. Hong, A. L. Antaris and H. Dai, Near-Infrared Fluorophores for Biomedical Imaging, *Nat. Biomed. Eng.*, 2017, **1**(1), 1–22, DOI: **10.1038/s41551-016-0010**.

13 C. Li, G. Chen, Y. Zhang, F. Wu and Q. Wang, Advanced Fluorescence Imaging Technology in the Near-Infrared-II Window for Biomedical Applications, *J. Am. Chem. Soc.*, 2020, **142**(35), 14789–14804, DOI: **10.1021/jacs.0c07022**.

14 C. Chen, R. Tian, Y. Zeng, C. Chu and G. Liu, Activatable Fluorescence Probes for "Turn-On" and Ratiometric

This journal is © The Royal Society of Chemistry 2024

J. Mater. Chem. C, 2024, **12**, 4369–4383 | **4379**

Biosensing and Bioimaging: From NIR-I to NIR-II, *Bioconjugate Chem.*, 2020, **31**(2), 276–292, DOI: **10.1021/acs.bioconjchem.9b00734**.

15 S. Wang, B. Li and F. Zhang, Molecular Fluorophores for Deep-Tissue Bioimaging, *ACS Cent. Sci.*, 2020, **6**(8), 1302–1316, DOI: **10.1021/acscentsci.0c00544**.

16 C. Chen and C. Fang, Devising Efficient Red-Shifting Strategies for Bioimaging: A Generalizable Donor–Acceptor Fluorophore Prototype, *Chem. – Asian J.*, 2020, **15**(10), 1514–1523, DOI: **10.1002/asia.202000175**.

17 H. Piwoński, S. Nozue and S. Habuchi, The Pursuit of Shortwave Infrared-Emitting Nanoparticles with Bright Fluorescence through Molecular Design and Excited-State Engineering of Molecular Aggregates, *ACS Nanosci. Au*, 2022, **2**(4), 253–283, DOI: **10.1021/acsnanoscienceau.1c00038**.

18 Z. Yang, X. Fan, X. Liu, Y. Chu, Z. Zhang, Y. Hu, H. Lin, J. Qian and J. Hua, Aggregation-Induced Emission Fluorophores Based on Strong Electron-Acceptor 2,2′-(Anthracene-9,10-Diylidene) Dimalononitrile for Biological Imaging in the NIR-II Window, *Chem. Commun.*, 2021, **57**(25), 3099–3102, DOI: **10.1039/D1CC00742D**.

19 Z. Lei and F. Zhang, Molecular Engineering of NIR-II Fluorophores for Improved Biomedical Detection, *Angew. Chem., Int. Ed.*, 2021, **60**(30), 16294–16308, DOI: **10.1002/anie.202007040**.

20 F. Ye, W. Chen, Y. Pan, S. H. Liu and J. Yin, Benzobisthiadiazoles: From Structure to Function, *Dyes Pigm.*, 2019, **171**, 107746, DOI: **10.1016/j.dyepig.2019.107746**.

21 U. Salzner, O. Karaltı and S. Durdaği, Does the Donor–Acceptor Concept Work for Designing Synthetic Metals?, *J. Mol. Model.*, 2006, **12**(5), 687–701, DOI: **10.1007/s00894-005-0046-2**.

22 P. Ü. Civcir, E. Özen and C. Karadeniz, Narrow-Energy Gap Conjugated Polymers Based on Benzobisthiadiazole and Thiadiazoloquinoxaline: DFT and TDDFT Study, *J. Mol. Model.*, 2020, **26**(10), 289, DOI: **10.1007/s00894-020-04541-y**.

23 B. Zhou, Z. Hu, Y. Jiang, C. Zhong, Z. Sun and H. Sun, Theoretical Exploitation of Acceptors Based on Benzobis(Thiadiazole) and Derivatives for Organic NIR-II Fluorophores, *Phys. Chem. Chem. Phys.*, 2018, **20**(30), 19759–19767, DOI: **10.1039/C8CP03135E**.

24 J. Qi, X. Zhou, D. Yang, W. Qiao, D. Ma and Z. Y. Wang, Optimization of Solubility, Film Morphology and Photodetector Performance by Molecular Side-Chain Engineering of Low-Bandgap Thienothiadiazole-Based Polymers, *Adv. Funct. Mater.*, 2014, **24**(48), 7605–7612, DOI: **10.1002/adfm.201401948**.

25 P. Sun, Y. Chen, B. Sun, H. Zhang, K. Chen, H. Miao, Q. Fan and W. Huang, Thienothiadiazole-Based NIR-II Dyes with D–A–D Structure for NIR-II Fluorescence Imaging Systems, *ACS Appl. Bio Mater.*, 2021, **4**(5), 4542–4548, DOI: **10.1021/acsabm.1c00274**.

26 M. Shimizu, R. Kaki, Y. Takeda, T. Hiyama, N. Nagai, H. Yamagishi and H. Furutani, 1,4-Bis(Diarylamino)-2,5-Bis(4-Cyanophenylethenyl)Benzenes: Fluorophores Exhibiting Efficient Red and Near-Infrared Emissions in Solid State, *Angew. Chem., Int. Ed.*, 2012, **51**(17), 4095–4099, DOI: **10.1002/anie.201108943**.

27 N. E. Sparks, S. M. Vijayan, J. K. Roy, A. Dorris, E. Lambert, D. Karunathilaka, N. I. Hammer, J. Leszczynski and D. L. Watkins, Synthesis and Characterization of Novel Thienothiadiazole-Based D−π−A−π−D Fluorophores as Potential NIR Imaging Agents, *ACS Omega*, 2023, **8**, 24513–24523, DOI: **10.1021/acsomega.3c02602**.

28 O. Kwon, S. Barlow, S. A. Odom, L. Beverina, N. J. Thompson, E. Zojer, J.-L. Brédas and S. R. Marder, Aromatic Amines: A Comparison of Electron-Donor Strengths, *J. Phys. Chem. A*, 2005, **109**(41), 9346–9352, DOI: **10.1021/jp054334s**.

29 Y. Yang, M. Xia, H. Zhao, S. Zhang and X. Zhang, A Cell-Surface-Specific Ratiometric Fluorescent Probe for Extracellular pH Sensing with Solid-State Fluorophore, *ACS Sens.*, 2018, **3**(11), 2278–2285, DOI: **10.1021/acssensors.8b00514**.

30 H. Yang, H. Mao, Z. Wan, A. Zhu, M. Guo, Y. Li, X. Li, J. Wan, X. Yang, X. Shuai and H. Chen, Micelles Assembled with Carbocyanine Dyes for Theranostic Near-Infrared Fluorescent Cancer Imaging and Photothermal Therapy, *Biomaterials*, 2013, **34**(36), 9124–9133, DOI: **10.1016/j.biomaterials.2013.08.022**.

31 T. Yanai, D. P. Tew and N. C. Handy, A New Hybrid Exchange–Correlation Functional Using the Coulomb-Attenuating Method (CAM-B3LYP), *Chem. Phys. Lett.*, 2004, **393**(1), 51–57, DOI: **10.1016/j.cplett.2004.06.011**.

32 T. H. Dunning, Gaussian Basis Sets for Use in Correlated Molecular Calculations. I. The Atoms Boron through Neon and Hydrogen, *J. Chem. Phys*, 1989, **90**(2), 1007–1023, DOI: **10.1063/1.456153**.

33 D. E. Woon and T. H. Dunning, Gaussian Basis Sets for Use in Correlated Molecular Calculations. III. The Atoms Aluminum through Argon, *J. Chem. Phys*, 1993, **98**(2), 1358–1371, DOI: **10.1063/1.464303**.

34 M. A. L. Marques and E. K. U. Gross, Time-Dependent Density Functional Theory, *Annu. Rev. Phys. Chem.*, 2004, **55**(1), 427–455, DOI: **10.1146/annurev.physchem.55.091602.094449**.

35 R. A. Kendall, T. H. Dunning and R. J. Harrison, Electron Affinities of the First-row Atoms Revisited. Systematic Basis Sets and Wave Functions, *J. Chem. Phys*, 1992, **96**(9), 6796–6806, DOI: **10.1063/1.462569**.

36 B. Mennucci, Polarizable Continuum Model, *Wiley Interdiscip. Rev.: Comput. Mol. Sci.*, 2012, **2**(3), 386–404, DOI: **10.1002/wcms.1086**.

37 R. L. Martin, Natural Transition Orbitals, *J. Chem. Phys*, 2003, **118**(11), 4775–4777, DOI: **10.1063/1.1558471**.

38 E. D. Glendening, C. R. Landis and F. Weinhold, Natural Bond Orbital Methods, *Wiley Interdiscip. Rev.: Comput. Mol. Sci.*, 2012, **2**(1), 1–42, DOI: **10.1002/wcms.51**.

39 *Ohio Supercomputer Center*, Ohio Supercomputer Center, **https://www.osc.edu/** (accessed 2023-03-09).

40 E. Epifanovsky, A. T. B. Gilbert, X. Feng, J. Lee, Y. Mao, N. Mardirossian, P. Pokhilko, A. F. White, M. P. Coons, A. L. Dempwolff, Z. Gan, D. Hait, P. R. Horn, L. D. Jacobson, I. Kaliman, J. Kussmann, A. W. Lange, K. U. Lao, D. S. Levine, J. Liu, S. C. McKenzie, A. F. Morrison, K. D. Nanda, F. Plasser, D. R. Rehn, M. L. Vidal, Z.-Q. You, Y. Zhu, B.

4380 | *J. Mater. Chem. C*, 2024, **12**, 4369–4383

This journal is © The Royal Society of Chemistry 2024

Alam, B. J. Albrecht, A. Aldossary, E. Alguire, J. H. Andersen, V. Athavale, D. Barton, K. Begam, A. Behn, N. Bellonzi, Y. A. Bernard, E. J. Berquist, H. G. A. Burton, A. Carreras, K. Carter-Fenk, R. Chakraborty, A. D. Chien, K. D. Closser, V. Cofer-Shabica, S. Dasgupta, M. de Wergifosse, J. Deng, M. Diedenhofen, H. Do, S. Ehlert, P.-T. Fang, S. Fatehi, Q. Feng, T. Friedhoff, J. Gayvert, Q. Ge, G. Gidofalvi, M. Goldey, J. Gomes, C. E. González-Espinoza, S. Gulania, A. O. Gunina, M. W. D. Hanson-Heine, P. H. P. Harbach, A. Hauser, M. F. Herbst, M. Hernández Vera, M. Hodecker, Z. C. Holden, S. Houck, X. Huang, K. Hui, B. C. Huynh, M. Ivanov, Á. Jász, H. Ji, H. Jiang, B. Kaduk, S. Kähler, K. Khistyaev, J. Kim, G. Kis, P. Klunzinger, Z. Koczor-Benda, J. H. Koh, D. Kosenkov, L. Koulias, T. Kowalczyk, C. M. Krauter, K. Kue, A. Kunitsa, T. Kus, I. Ladjánszki, A. Landau, K. V. Lawler, D. Lefrancois, S. Lehtola, R. R. Li, Y.-P. Li, J. Liang, M. Liebenthal, H.-H. Lin, Y.-S. Lin, F. Liu, K.-Y. Liu, M. Loipersberger, A. Luenser, A. Manjanath, P. Manohar, E. Mansoor, S. F. Manzer, S.-P. Mao, A. V. Marenich, T. Markovich, S. Mason, S. A. Maurer, P. F. McLaughlin, M. F. S. J. Menger, J.-M. Mewes, S. A. Mewes, P. Morgante, J. W. Mullinax, K. J. Oosterbaan, G. Paran, A. C. Paul, S. K. Paul, F. Pavošević, Z. Pei, S. Prager, E. I. Proynov, Á. Rák, E. Ramos-Cordoba, B. Rana, A. E. Rask, A. Rettig, R. M. Richard, F. Rob, E. Rossomme, T. Scheele, M. Scheurer, M. Schneider, N. Sergueev, S. M. Sharada, W. Skomorowski, D. W. Small, C. J. Stein, Y.-C. Su, E. J. Sundstrom, Z. Tao, J. Thirman, G. J. Tornai, T. Tsuchimochi, N. M. Tubman, S. P. Veccham, O. Vydrov, J. Wenzel, J. Witte, A. Yamada, K. Yao, S. Yeganeh, S. R. Yost, A. Zech, I. Y. Zhang, X. Zhang, Y. Zhang, D. Zuev, A. Aspuru-Guzik, A. T. Bell, N. A. Besley, K. B. Bravaya, B. R. Brooks, D. Casanova, J.-D. Chai, S. Coriani, C. J. Cramer, G. Cserey, A. E. DePrince III, R. A. DiStasio Jr, A. Dreuw, B. D. Dunietz, T. R. Furlani, W. A. Goddard III, S. Hammes-Schiffer, T. Head-Gordon, W. J. Hehre, C.-P. Hsu, T.-C. Jagau, Y. Jung, A. Klamt, J. Kong, D. S. Lambrecht, W. Liang, N. J. Mayhall, C. W. McCurdy, J. B. Neaton, C. Ochsenfeld, J. A. Parkhill, R. Peverati, V. A. Rassolov, Y. Shao, L. V. Slipchenko, T. Stauch, R. P. Steele, J. E. Subotnik, A. J. W. Thom, A. Tkatchenko, D. G. Truhlar, T. Van Voorhis, T. A. Wesolowski, K. B. Whaley, H. L. Woodcock, III, P. M. Zimmerman, S. Faraji, P. M. W. Gill, M. Head-Gordon, J. M. Herbert and A. I. Krylov, Software for the Frontiers of Quantum Chemistry: An Overview of Developments in the Q-Chem 5 Package, *J. Chem. Phys.*, 2021, **155**(8), 084801, DOI: **10.1063/5.0055522**.

41 E. D. Cosco, J. R. Caram, O. T. Bruns, D. Franke, R. A. Day, E. P. Farr, M. G. Bawendi and E. M. Sletten, Flavylium Polymethine Fluorophores for Near- and Shortwave Infrared Imaging, *Angew. Chem., Int. Ed.*, 2017, **56**(42), 13126–13129, DOI: **10.1002/anie.201706974**.

42 M. Levitus, Tutorial: Measurement of Fluorescence Spectra and Determination of Relative Fluorescence Quantum Yields of Transparent Samples, *Methods Appl. Fluoresc.*, 2020, **8**(3), 033001, DOI: **10.1088/2050-6120/ab7e10**.

43 Z. Yuan, C. Lin, Y. He, B. Tao, M. Chen, J. Zhang, P. Liu and K. Cai, Near-Infrared Light-Triggered Nitric-Oxide-Enhanced Photodynamic Therapy and Low-Temperature Photothermal Therapy for Biofilm Elimination, *ACS Nano*, 2020, **14**(3), 3546–3562, DOI: **10.1021/acsnano.9b09871**.

44 S. Park, W. J. Lee, S. Park, D. Choi, S. Kim and N. Park, Reversibly pH-Responsive Gold Nanoparticles and Their Applications for Photothermal Cancer Therapy, *Sci. Rep.*, 2019, **9**(1), 20180, DOI: **10.1038/s41598-019-56754-8**.

45 M. Lin, C. Guo, J. Li, D. Zhou, K. Liu, X. Zhang, T. Xu, H. Zhang, L. Wang and B. Yang, Polypyrrole-Coated Chain-like Gold Nanoparticle Architectures with the 808 Nm Photothermal Transduction Efficiency up to 70%, *ACS Appl. Mater. Interfaces*, 2014, **6**(8), 5860–5868, DOI: **10.1021/am500715f**.

46 C. M. Chism, S. Plash, D. Zuckerman, G. S. Dasanayake, M. Bennett, S. K. Tripathi, S. D. Pedigo and E. E. L. Tanner, Antimicrobial Effects of Anion Manipulation with Biocompatible Choline Carboxylic Acid-Based Ionic Liquids, *ACS Appl. Eng. Mater.*, 2023, **1**(1), 23–31, DOI: **10.1021/acsaenm.2c00004**.

47 C. M. Hamadani, I. Chandrasiri, M. L. Yaddehige, G. S. Dasanayake, I. Owolabi, A. Flynt, M. Hossain, L. Liberman, T. P. Lodge, T. A. Werfel, D. L. Watkins and E. E. L. Tanner, Improved Nanoformulation and Bio-Functionalization of Linear-Dendritic Block Copolymers with Biocompatible Ionic Liquids, *Nanoscale*, 2022, **14**(16), 6021–6036, DOI: **10.1039/D2NR00538G**.

48 C. M. Hamadani, M. J. Goetz, S. Mitragotri and E. E. L. Tanner, Protein-Avoidant Ionic Liquid (PAIL)–Coated Nanoparticles to Increase Bloodstream Circulation and Drive Biodistribution, *Sci. Adv.*, 2020, **6**(48), eabd7563, DOI: **10.1126/sciadv.abd7563**.

49 C. M. Hamadani, G. S. Dasanayake, M. E. Gorniak, M. C. Pride, W. Monroe, C. M. Chism, R. Heintz, E. Jarrett, G. Singh, S. X. Edgecomb and E. E. L. Tanner, Development of Ionic Liquid-Coated PLGA Nanoparticles for Applications in Intravenous Drug Delivery, *Nat. Protoc.*, 2023, **18**(8), 2509–2557, DOI: **10.1038/s41596-023-00843-6**.

50 Y. Zhang, S. A. Autry, L. E. McNamara, S. T. Nguyen, N. Le, P. Brogdon, D. L. Watkins, N. I. Hammer and J. H. Delcamp, Near-Infrared Fluorescent Thienothiadiazole Dyes with Large Stokes Shifts and High Photostability, *J. Org. Chem.*, 2017, **82**(11), 5597–5606, DOI: **10.1021/acs.joc.7b00422**.

51 S. Steinberger, A. Mishra, E. Reinold, E. Mena-Osteritz, H. Müller, C. Uhrich, M. Pfeiffer and P. Bäuerle, Synthesis and Characterizations of Red/near-IR Absorbing A–D–A–D–A-Type Oligothiophenes Containing Thienothiadiazole and Thienopyrazine Central Units, *J. Mater. Chem.*, 2012, **22**(6), 2701–2712, DOI: **10.1039/C2JM13285K**.

52 L. Wu, X. Li, Y. Ling, C. Huang and N. Jia, Morpholine Derivative-Functionalized Carbon Dots-Based Fluorescent Probe for Highly Selective Lysosomal Imaging in Living Cells, *ACS Appl. Mater. Interfaces*, 2017, **9**(34), 28222–28232, DOI: **10.1021/acsami.7b08148**.

This journal is © The Royal Society of Chemistry 2024

J. Mater. Chem. C, 2024, **12**, 4369–4383 | **4381**

53 M. Das, B. Koley, U. K. Das, A. Bag, S. Laha, B. Chandra Samanta, I. Choudhuri, N. Bhattacharyya and T. Maity, Piperidine Based Effective Chemosensor for Zn(ɪɪ) with the Formation of Binuclear Zn Complex Having Specific Al(ɪɪɪ) Detection Ability in Aqueous Medium and Live Cell Images, *J. Photochem. Photobiol. Chem.*, 2021, **415**, 113302, DOI: **10.1016/j.jphotochem.2021.113302**.

54 I. Chandrasiri, M. Loku Yaddehige, B. Li, Y. Sun, W. E. Meador, A. Dorris, M. Farid Zia, N. I. Hammer, A. Flynt, J. H. Delcamp, E. Davis, A. Lippert and D. L. Watkins, Cross-Linking Poly(Caprolactone)–Polyamidoamine Linear Dendritic Block Copolymers for Theranostic Nanomedicine, *ACS Appl. Polym. Mater.*, 2022, **4**(5), 2972–2986, DOI: **10.1021/acsapm.1c01131**.

55 S.-Y. Kim, Y.-J. Cho, A.-R. Lee, H. Son, W.-S. Han, D. W. Cho and S. O. Kang, Influence of π-Conjugation Structural Changes on Intramolecular Charge Transfer and Photoinduced Electron Transfer in Donor–π–Acceptor Dyads, *Phys. Chem. Chem. Phys.*, 2016, **19**(1), 426–435, DOI: **10.1039/C6CP06566J**.

56 C. Bora and S. K. Dolui, Fabrication of Polypyrrole/Graphene Oxide Nanocomposites by Liquid/Liquid Interfacial Polymerization and Evaluation of Their Optical, Electrical and Electrochemical Properties, *Polymer*, 2012, **53**(4), 923–932, DOI: **10.1016/j.polymer.2011.12.054**.

57 J. Mu, M. Xiao, Y. Shi, X. Geng, H. Li, Y. Yin and X. Chen, The Chemistry of Organic Contrast Agents in the NIR-II Window, *Angew. Chem., Int. Ed.*, 2022, **61**(14), e202114722, DOI: **10.1002/anie.202114722**.

58 Y. Li, T. Ren and W.-J. Dong, Tuning Photophysical Properties of Triphenylamine and Aromatic Cyano Conjugate-Based Wavelength-Shifting Compounds by Manipulating Intramolecular Charge Transfer Strength, *J. Photochem. Photobiol. Chem.*, 2013, **251**, 1–9, DOI: **10.1016/j.jphotochem.2012.10.002**.

59 J. Wang and B. Durbeej, How Accurate Are TD-DFT Excited-State Geometries Compared to DFT Ground-State Geometries?, *J. Comput. Chem.*, 2020, **41**(18), 1718–1729, DOI: **10.1002/jcc.26213**.

60 I. Chandrasiri, D. G. Abebe, M. Loku Yaddehige, J. S. D. Williams, M. F. Zia, A. Dorris, A. Barker, B. L. Simms, A. Parker, B. P. Vinjamuri, N. Le, J. N. Gayton, M. B. Chougule, N. I. Hammer, A. Flynt, J. H. Delcamp and D. L. Watkins, Self-Assembling PCL–PAMAM Linear Dendritic Block Copolymers (LDBCs) for Bioimaging and Phototherapeutic Applications, *ACS Appl. Bio Mater.*, 2020, **3**(9), 5664–5677, DOI: **10.1021/acsabm.0c00432**.

61 Y. Du, N. Alifu, Z. Wu, R. Chen, X. Wang, G. Ji, Q. Li, J. Qian, B. Xu and D. Song, Encapsulation-Dependent Enhanced Emission of Near-Infrared Nanoparticles Using *in Vivo* Three-Photon Fluorescence Imaging, *Front. Bioeng. Biotechnol*, 2020, **8**, 1029.

62 D. B. Sulas, A. E. London, L. Huang, L. Xu, Z. Wu, T. N. Ng, B. M. Wong, C. W. Schlenker, J. D. Azoulay and M. Y. Sfeir, Preferential Charge Generation at Aggregate Sites in Narrow Band Gap Infrared Photoresponsive Polymer Semiconductors, *Adv. Opt. Mater.*, 2018, **6**(7), 1701138, DOI: **10.1002/adom.201701138**.

63 K. N. Clayton, J. W. Salameh, S. T. Wereley and T. L. Kinzer-Ursem, Physical Characterization of Nanoparticle Size and Surface Modification Using Particle Scattering Diffusometry, *Biomicrofluidics*, 2016, **10**(5), 054107, DOI: **10.1063/1.4962992**.

64 X. Zeng, Y. Xiao, J. Lin, S. Li, H. Zhou, J. Nong, G. Xu, H. Wang, F. Xu, J. Wu, Z. Deng and X. Hong, Near-Infrared II Dye-Protein Complex for Biomedical Imaging and Imaging-Guided Photothermal Therapy, *Adv. Healthcare Mater*, 2018, **7**(18), 1800589, DOI: **10.1002/adhm.201800589**.

65 J. Li and K. Pu, Development of Organic Semiconducting Materials for Deep-Tissue Optical Imaging, Phototherapy and Photoactivation, *Chem. Soc. Rev.*, 2019, **48**(1), 38–71, DOI: **10.1039/C8CS00001H**.

66 P. Zhang, H. Huang, J. Huang, H. Chen, J. Wang, K. Qiu, D. Zhao, L. Ji and H. Chao, Noncovalent Ruthenium(ɪɪ) Complexes-Single-Walled Carbon Nanotube Composites for Bimodal Photothermal and Photodynamic Therapy with Near-Infrared Irradiation, *ACS Appl. Mater. Interfaces*, 2015, **7**(41), 23278–23290, DOI: **10.1021/acsami.5b07510**.

67 P. Murto, A. Minotto, A. Zampetti, X. Xu, M. R. Andersson, F. Cacialli and E. Wang, Triazolobenzothiadiazole-Based Copolymers for Polymer Light-Emitting Diodes: Pure Near-Infrared Emission *via* Optimized Energy and Charge Transfer, *Adv. Opt. Mater.*, 2016, **4**(12), 2068–2076, DOI: **10.1002/adom.201600483**.

68 J. Kulhánek, O. Pytela, F. Bureš and M. Klikar, Small Heterocyclic D-π-D-π-A Push–Pull Molecules with Complex Electron Donors, *Eur. J. Org. Chem.*, 2021, 3223–3233, DOI: **10.1002/ejoc.202100137**.

69 J. Qi, X. Duan, Y. Cai, S. Jia, C. Chen, Z. Zhao, Y. Li, H.-Q. Peng, R. T. Kwok, J. W. Lam, D. Ding and B. Zhong Tang, Simultaneously Boosting the Conjugation, Brightness and Solubility of Organic Fluorophores by Using AIEgens, *Chem. Sci.*, 2020, **11**(32), 8438–8447, DOI: **10.1039/D0SC03423A**.

70 A. Thomas, C. Ji, B. Siddlingeshwar, P. U. Manohar, F. Ying and W. Wu, Revealing the Biradicaloid Nature Inherited in the Derivatives of Thieno[3,4][1,2,5]Thiadiazole: A Computational Study, *Phys. Chem. Chem. Phys.*, 2021, **23**(2), 1050–1061, DOI: **10.1039/D0CP05106C**.

71 J. D. Yuen, M. Wang, J. Fan, D. Sheberla, M. Kemei, N. Banerji, M. Scarongella, S. Valouch, T. Pho, R. Kumar, E. C. Chesnut, M. Bendikov and F. Wudl, Importance of Unpaired Electrons in Organic Electronics, *J. Polym. Sci. Part Polym. Chem.*, 2015, **53**(2), 287–293, DOI: **10.1002/pola.27321**.

72 S. P. Anthony, Organic Solid-State Fluorescence: Strategies for Generating Switchable and Tunable Fluorescent Materials, *ChemPlusChem*, 2012, **77**(7), 518–531, DOI: **10.1002/cplu.201200073**.

73 J. L. Bahr, G. Kodis, L. de la Garza, S. Lin, A. L. Moore, T. A. Moore and D. Gust, Photoswitched Singlet Energy Transfer in a Porphyrin−Spiropyran Dyad, *J. Am. Chem. Soc.*, 2001, **123**(29), 7124–7133, DOI: **10.1021/ja010058t**.

4382 | *J. Mater. Chem. C*, 2024, **12**, 4369–4383

This journal is © The Royal Society of Chemistry 2024

74 R. Radhakrishnan and K. G. Sreejalekshmi, Computational Design, Synthesis, and Structure Property Evaluation of 1,3-Thiazole-Based Color-Tunable Multi-Heterocyclic Small Organic Fluorophores as Multifunctional Molecular Materials, *J. Org. Chem.*, 2018, **83**(7), 3453–3466, DOI: **10.1021/acs.joc.7b02978**.

75 H. Dai, Q. Shen, J. Shao, W. Wang, F. Gao and X. Dong, Small Molecular NIR-II Fluorophores for Cancer Phototheranostics, *Innovation*, 2021, **2**(1), 100082, DOI: **10.1016/j.xinn.2021.100082**.

76 T. V. Duncan, K. Susumu, L. E. Sinks and M. J. Therien, Exceptional Near-Infrared Fluorescence Quantum Yields and Excited-State Absorptivity of Highly Conjugated Porphyrin Arrays, *J. Am. Chem. Soc.*, 2006, **128**(28), 9000–9001, DOI: **10.1021/ja061897o**.

77 S. H. Lin, Rate of Interconversion of Electronic and Vibrational Energy, *J. Chem. Phys.*, 2004, **44**(10), 3759–3767, DOI: **10.1063/1.1726531**.

78 S. He, J. Song, J. Qu and Z. Cheng, Crucial Breakthrough of Second Near-Infrared Biological Window Fluorophores: Design and Synthesis toward Multimodal Imaging and Theranostics, *Chem. Soc. Rev.*, 2018, **47**(12), 4258–4278, DOI: **10.1039/C8CS00234G**.

79 V. Rosiuk, A. Runser, A. Klymchenko and A. Reisch, Controlling Size and Fluorescence of Dye-Loaded Polymer Nanoparticles through Polymer Design, *Langmuir*, 2019, **35**(21), 7009–7017, DOI: **10.1021/acs.langmuir.9b00721**.

80 R. Ahmed and A. K. Manna, Understanding High Fluorescence Quantum Yield and Simultaneous Large Stokes Shift in Phenyl Bridged Donor−π–Acceptor Dyads with Varied Bridge Lengths in Polar Solvents, *J. Phys. Chem. A*, 2022, **126**(26), 4221–4229, DOI: **10.1021/acs.jpca.2c02950**.

81 J. Hoche, A. Schulz, L. M. Dietrich, A. Humeniuk, M. Stolte, D. Schmidt, T. Brixner, F. Würthner and R. Mitric, The Origin of the Solvent Dependence of Fluorescence Quantum Yields in Dipolar Merocyanine Dyes, *Chem. Sci.*, 2019, **10**(48), 11013–11022, DOI: **10.1039/C9SC05012D**.

82 K. K. Amponsah-Efah, P. Mistry, R. Eisenhart and R. Suryanarayanan, The Influence of the Strength of Drug–Polymer Interactions on the Dissolution of Amorphous Solid Dispersions, *Mol. Pharmaceutics*, 2021, **18**(1), 174–186, DOI: **10.1021/acs.molpharmaceut.0c00790**.

83 J. M. Morachis, E. A. Mahmoud and A. Almutairi, Physical and Chemical Strategies for Therapeutic Delivery by Using Polymeric Nanoparticles, *Pharmacol. Rev.*, 2012, **64**(3), 505–519, DOI: **10.1124/pr.111.005363**.

84 J. W. Hickey, J. L. Santos, J.-M. Williford and H.-Q. Mao, Control of Polymeric Nanoparticle Size to Improve Therapeutic Delivery, *J. Controlled Release*, 2015, **219**, 536–547, DOI: **10.1016/j.jconrel.2015.10.006**.

85 M. Vogel, W. Rettig, U. Fiedeldei and H. Baumgärtel, Non-Radiative Deactivation *via* Biradicaloid Charge-Transfer States in Oxazine and Thiazine Dyes, *Chem. Phys. Lett.*, 1988, **148**(4), 347–352, DOI: **10.1016/0009-2614(88)87286-5**.

86 W. Rettig and R. Gleiter, Dependence of Intramolecular Rotation in *P*-Cyano-*N*,*N*-Dialkylanilines on the Twist Angle. A Fluorescence, UV Absorption, and Photoelectron Spectroscopic Study, *J. Phys. Chem.*, 1985, **89**(22), 4676–4680, DOI: **10.1021/j100268a006**.

87 W. Rettig, Charge Separation in Excited States of Decoupled Systems—TICT Compounds and Implications Regarding the Development of New Laser Dyes and the Primary Process of Vision and Photosynthesis, *Angew. Chem., Int. Ed. Engl.*, 1986, **25**(11), 971–988, DOI: **10.1002/anie.198609711**.

88 C. Wang, W. Chi, Q. Qiao, D. Tan, Z. Xu and X. Liu, Twisted Intramolecular Charge Transfer (TICT) and Twists beyond TICT: From Mechanisms to Rational Designs of Bright and Sensitive Fluorophores, *Chem. Soc. Rev.*, 2021, **50**(22), 12656–12678, DOI: **10.1039/D1CS00239B**.

89 M. J. Mitchell, M. M. Billingsley, R. M. Haley, M. E. Wechsler, N. A. Peppas and R. Langer, Engineering Precision Nanoparticles for Drug Delivery, *Nat. Rev. Drug Discovery*, 2021, **20**(2), 101–124, DOI: **10.1038/s41573-020-0090-8**.

90 S. Sharma, R. Parveen and B. P. Chatterji, Toxicology of Nanoparticles in Drug Delivery, *Curr. Pathobiol. Rep.*, 2021, **9**(4), 133–144, DOI: **10.1007/s40139-021-00227-z**.

91 A. B. Sairam, A. Sanmugam, A. Pushpparaj, G. Mahesh Kumar, N. Sundarapandian, S. Balaji, M. Nallal and K. H. Park, Toxicity of Polymeric Nanodrugs as Drug Carriers, *ACS Chem. Health Saf.*, 2023, **30**, 236–250.

92 S. Nomura, Y. Morimoto, H. Tsujimoto, M. Arake, M. Harada, D. Saitoh, I. Hara, E. Ozeki, A. Satoh, E. Takayama, K. Hase, Y. Kishi and H. Ueno, Highly Reliable, Targeted Photothermal Cancer Therapy Combined with Thermal Dosimetry Using a near-Infrared Absorbent, *Sci. Rep.*, 2020, **10**(1), 9765, DOI: **10.1038/s41598-020-66646-x**.